PHYSICAL REVIEW MATERIALS **4**, 065002 (2020)

Atomic locations of minor dopants and their roles in the stabilization of η-Cu_6Sn_5

Wenhui Yang,[1,*] Xuan Quy Tran,[1] Tomokazu Yamamoto,[1,2] Satoru Yoshioka,[1] Flora Somidin,[3]
Kazuhiro Nogita,[3] and Syo Matsumura[1,2]
[1]*Department of Applied Quantum Physics and Nuclear Engineering, Kyushu University, Motooka 744, Nishi-ku, Fukuoka 819-0395, Japan*
[2]*The Ultramicroscopy Research Center, Kyushu University, Motooka 744, Nishi-ku, Fukuoka 819-0395, Japan*
[3]*Nihon Superior Centre for the Manufacture of Electronic Materials (NS CMEM), School of Mechanical and Mining Engineering,*
The University of Queensland, Brisbane QLD 4072, Australia

(Received 14 January 2020; accepted 26 May 2020; published 17 June 2020)

Chemical modification using only small amounts of elements such as Zn, In, Sb, or Ni has proven to be an effective means to control the desirable crystal structure of hexagonal η-Cu_6Sn_5 over a wide thermally operating window, typically found in Pb-free Sn-based soldering or Li-ion battery anode applications. Though appealing, the underlying mechanisms on the role of these dopants remain incomplete and their atomic arrangements within the η-Cu_6Sn_5 lattices have not yet been experimentally determined. In the current study, we directly reveal the atomic positions of Zn, In, and Sb at the *Sn* sites of η-Cu_6Sn_5 via atomic-scale x-ray energy dispersive spectroscopy (XEDS) maps utilizing advanced Cs-corrected scanning transmission electron microscopy. The use of advanced statistical algorithms including Poisson non-local principal component analysis and lattice averaging enables the fine resolution of weak XEDS maps from trace dopant elements. Our first-principles calculations further identify the influence of dopants at these atomic sites on the overall energetics, electronic structures, as well as local bonding environments, leading to the most favorable situations for η-Cu_6Sn_5 stabilization.

DOI: 10.1103/PhysRevMaterials.4.065002

I. INTRODUCTION

Due to environmental concerns, Pb-free Sn-based solders have been widely used for solder interconnects in electronics packaging applications [1,2]. It is also well known that the intermetallic compound (IMC) Cu_6Sn_5 which forms between Cu substrates and Sn-based solders during the soldering process significantly influences the resultant joint properties [3]. This may be largely attributed to the complex phase-change behavior of Cu_6Sn_5 that is highly dependent on the local composition and thermal processing conditions. Of the five crystal structure variants reported to date, i.e., η, η', η^6, η^8, η^{4+1} [4–6], Cu_6Sn_5 commonly crystallizes in a hexagonal structure η ($P6_3/mmc$) above 186 °C, and undergoes a phase transformation into a monoclinic structure η' ($C2/c$) when cooling below 186 °C [7]. The transformation reportedly causes about 2.15% volumetric expansion, leading to significant stress generation and cracking, and potentially compromises the structural reliability of solder joints [8].

Chemical modifications via elemental doping or alloying are often used to control the desirable phase compositions and structures in intermetallic and alloys [9]. For instance, Nogita *et al.* [10] reported that only a small addition of 0.05 wt % Ni in Sn-0.7wt%Cu is sufficient to stabilize the high-temperature η-Cu_6Sn_5 phase down to room temperature, thus bypassing the undesirable $\eta \rightarrow \eta'$ phase transition at 186 °C and its associated volumetric change during soldering processes. Other benefits also include microstructural refinement [11], good fluidity during soldering [12–14], improved mechanical properties of solder joints [15,16], etc. The same strategy has also been applied successfully when using Zn or In as chemical dopants for the stabilization of η-Cu_6Sn_5 [17,18].

In addition, Cu_6Sn_5 has been regarded as a potential candidate for Li-ion battery anode applications [19,20]. Since η-Cu_6Sn_5 exhibits a theoretical capacity of 358 mAh/g when fully lithiated to $Li_{13}Cu_6Sn_5$, this performance is comparable with that of the commonly used graphite anodes (372 mAh/g) [19]. Furthermore, during an electrochemical reaction, Cu in Cu_6Sn_5 acts as a stress buffer against the significant volumetric change due to *Sn* lithiation/delithiation, thus remarkably improving the overall cyclic charge/discharge stability compared to a pure *Sn* anode [20]. As a result, numerous studies have been dedicated to exploring the battery performance of Cu_6Sn_5 anodes with respect to various fabrication methods [21,22], compositions [23,24], or anode architectures [25].

Though appealing for various soldering or battery applications, fundamental understanding on the role of many chemical dopants in Cu_6Sn_5 remains unclear, especially as their atomic arrangements within the Cu_6Sn_5 lattices are still experimentally unidentified. Theoretically, several studied have been performed to predict the atomic locations of dopants via screening the most favorable energetics and electronic structures using first-principles calculations, yet the results are incomplete given the lack of experimental validation. For instance, Schwingenschlögl *et al.* [26] propose *Cu*2 sites of η-Cu_6Sn_5 as the most favorable location for Ni while Zeng *et al.* [18,27] postulate the occupancy of In and Zn dopants at the *Sn* sites. In view of the classical Hume-Rothery rule, the previous predictions for Ni and In seem reasonable considering the relatively close positions between the dopant and host elements on the periodic table as well as their atomic

---

[*] Corresponding author: yangwenhui@nucl.kyushu-u.ac.jp

TABLE I. Nominal compositions of the samples.

Element/at. %	Cu	Sn	Zn	In	Sb
$Cu_6(Sn, Zn)_5$	54.5	41.0	4.5		
$Cu_6(Sn, In)_5$	54.5	41.0		4.5	
$Cu_6(Sn, Sb)_5$	54.5	41.0			4.5

sizes, valence electron configurations, and so forth. However, the argument is less clear in the case of Zn substituting for *Sn* despite its proximity to Cu on the periodic table. This leaves an important gap in our current understanding on the underlying mechanism of chemical dopant-induced phase stabilization in η-Cu_6Sn_5.

Motivated by previous studies, recently we have provided direct experimental evidence on the atomic positions of Ni at the Wyckoff *Cu*2 sites in η-Cu_6Sn_5 utilizing atomic-resolution x-ray energy-dispersive spectroscopy (XEDS) on a Cs-corrected scanning transmission electron microscope (STEM) [28], thereby confirming the accuracy of the first-principles calculations by other authors [26]. To develop a more complete picture, herein we systematically explore the atomic positions of various dopants including Zn, In, and Sb in η-Cu_6Sn_5 using the previously established methodology. The results are further supported in terms of energetics, electronic properties, and chemical bonding analysis within the framework of density functional theory (DFT).

II. MATERIALS AND METHODS

A. Sample preparation

$Cu_6(Sn, Zn)_5$, $Cu_6(Sn, In)_5$, and $Cu_6(Sn, Sb)_5$ alloy samples were prepared with nominal compositions shown in Table I by direct alloying of high purity (99.99 wt %) Cu, Sn, Zn, In, and Sb metal wires in a sealed quartz ampoule under a vacuum condition of 10^{-3} Torr. The sealed ampoule was first heated at 900 °C in an electric resistance furnace for 24 h and then quenched in iced water. Subsequent annealing was applied at 380 °C for 480 h followed by 160 °C for 72 h to facilitate structural and compositional homogeneity. Bulk samples of about $4\times4\times2\ \mathrm{mm}^3$ in size were then obtained from the as-annealed alloys for structural characterization.

Lamella samples thinner than ~100 nm were prepared by means of focused ion beam (FIB) (dual beam SEM-FIB, HITACHI MI4000L). The final FIB thinning process was operated at an acceleration voltage of 10 kV and an ion-beam current of 96 pA. Mo grids were used for supporting the lamella samples without generation of background x-ray peaks overlapping with characteristic x rays from elements such as Cu, Sn, etc. in subsequent analysis. Prior to structural characterization, the lamella samples were further polished using argon-ion milling (Fischione Nano Mill Model 1040) to remove contaminants as well as damaged layers from the previous process.

B. Atomic-scale STEM imaging, elemental mapping, and data analysis

Structural characterization was performed using a Cs-corrected scanning transmission electron microscope (STEM, JEOL-JEM ARM200CF) operated at an acceleration voltage of 200 kV with a low background beryllium holder (JEOL EM-01040RSTHB). The instrument is also equipped with a dual-Silicon Drift Detector system having a collection solid angle of approximately 1.8 steradian (sr) which offers highly efficient acquisition of x rays and energy resolution (~130 eV). We conducted STEM imaging in both high-angle annular dark-field (HAADF) and annular bright-field (ABF) modes. The corresponding annular detection ranges settings were 90–180 and 9–25 mrad, respectively. To minimize the effect of thermal and mechanical drifts during image acquisition, a series of multiple fast scanned images (1024×1024 pixels) was first acquired from an area of interest with a dwell time of 1 μs/pixel and followed by cross correlation to form the final image.

In addition, atomic-resolution x-ray energy-dispersive spectroscopy (XEDS) was carried out with a fine STEM probe current of 34 pA. To improve the signal-to-noise ratio (SNR) of the trace elements, here we employed two denoising algorithms for postprocessing the original XEDS maps: (i) Poisson nonlocal principal component analysis (NLPCA), and (ii) lattice averaging combined with Gaussian smoothing. These methods can effectively resolve a trace amount of Ni as low as 5 at. % in η-Cu_6Sn_5 as shown in our previous publication [28]. In the NLPCA approach [29,30], an original XEDS map (1024×1024 pixels) was first divided into a collection of small noisy patches (32×32 pixels). The resultant patches were then grouped into a total of ten clusters and were processed by principal component analysis (PCA). Finally, the denoised patches were recombined to form a denoised image. The technique is also sensitive to local compositional variations, thus would be suitable for cases where the dopants are heterogeneously distributed throughout the parent lattice. Alternatively, we also applied the lattice-averaging method to improve the effective counts per pixel of the original maps. With a focus on the lattice location of constituent atoms within the crystal unit cell rather than the coarse distribution of elements, this approach divides an XEDS map (1024×1024 pixels) into equally two-dimensional (2D) projected unit-cell patches (40×50 pixels) and directly overlays each other to form an averaged image with improved SNR [31]. Deconvolution of XEDS spectra between neighbor elements on the periodic table, for example, In *L* (3.286 keV), Sb *L* (3.604 keV), and *Sn L* (3.444 keV), was also performed.

C. First-principles calculations

Using the experimental crystal structure of η-Cu_6Sn_5 ($a = 4.190$ Å, $c = 5.086$ Å, $c/a = 1.214$) as a starting structure [32], a hexagonal (hcp) supercell of $2\times2\times5$ units containing 48 Cu and 40 *Sn* atoms was used to model the binary η-Cu_6Sn_5 (space group $P6_3/mmc$) as shown Fig. 1. In this initial structure, Cu atoms are located at two different crystallographically inequivalent Wyckoff sites, namely *Cu*1 (2*a*) and *Cu*2 (2*d*), with the corresponding Cu occupancy of 100% and 20%, respectively. Note that the spatial distribution of *Cu*2 sites is random in nature and our study is not exhaustive of all the possible configurations but rather is a representative case of *Cu*2 site arrangement within the η-Cu_6Sn_5 $2\times2\times5$ supercells. In Fig. 1, all possible arrangements of *Cu*2 sites are

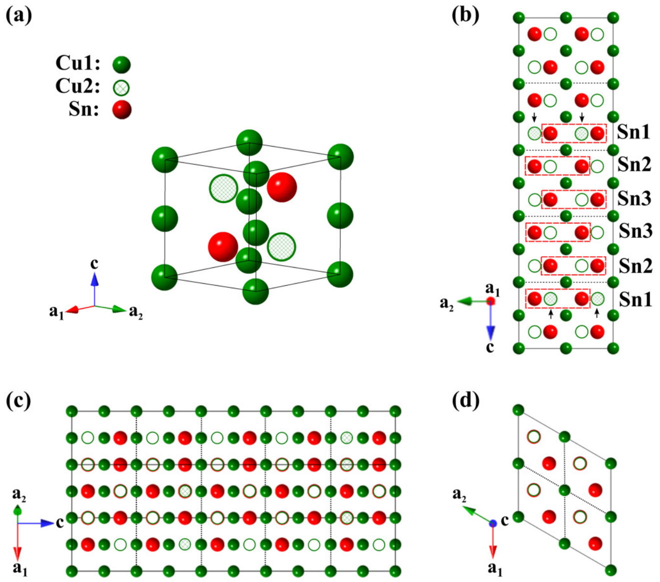

FIG. 1. A 3D unit cell of η-Cu_6Sn_5 (a), 2D views of a 2×2×5 supercell of η-Cu_6Sn_5 along different orientations (b) $[2\bar{1}\bar{1}0]$, (c) $[01\bar{1}0]$, and (d) [0001].

indicated by green open circles while only those occupied by Cu atoms are marked by black arrows. For ease of discussion, the three equivalent Wyckoff *Sn* sites (2*c*) can be further classified into *Sn*1, *Sn*2, and *Sn*3 sites depending on their relative positions to the *Cu*2 sites as illustrated in Fig. 1(b). To simulate the effect of doping, either *Cu*1, *Cu*2, or *Sn* sites were systematically substituted by 4.5 at. % dopants of Zn, In, Sb, or Ni according to the experimental compositions. In addition, a unit cell of η'-Cu_6Sn_5 with the monoclinic structure (space group $C2/c$, $a = 11.036$ Å, $b = 7.288$ Å, $c = 9.841$ Å, $\beta = 98.81^\circ$ [4]) containing 24 Cu and 20 *Sn* atoms was also used for comparison with the η-Cu_6Sn_5 (Fig. S1 in Ref. [33]). This structural setting consists of seven different Wyckoff sites, namely, *Cu*1′, *Cu*2′, *Cu*3′, *Cu*4′, *Sn*1′, *Sn*2′, and *Sn*3′ (Table S1 in Ref. [33]). We note that the *Cu*4′ sites in η'-Cu_6Sn_5 are crystallographically equivalent to the *Cu*2 sites in η-Cu_6Sn_5, however, there are no direct correlations between each of the *Sn* sites in η' and those in η. Equivalent amounts (4.5 at. %) of Zn, In, Sb, or Ni dopants were also applied for the η'-Cu_6Sn_5.

Density functional theory (DFT) calculations were carried out using the projector augmented wave (PAW) method as implemented within the Vienna abinitio simulation package (VASP). Generalized gradient approximations (GGA) for the exchange–correlation functional were applied using the Perdew, Burke, and Ernzerhof (PBE) formulation. The plane-wave cutoff energy was 400 eV. The gamma-centered schemes (9×9×3 and 11×11×11) were used for *k*-point sampling of the Brillouin zones in η-Cu_6Sn_5 and η'-Cu_6Sn_5, respectively. Full optimization of lattice parameters and ionic positions was performed within the self-consistent field and force convergence thresholds of 10^{-6} and 0.01 eV/atom, respectively. For the calculations of density of states (DOS), the *k*-point grids were further refined to 21×21×7. In the standard PAW potentials, the valence electronic configurations for each atomic type are represented as follows: Cu: $3d^{10}4p^1$, Sn: $5s^25p^2$, Zn: $3d^{10}4p^2$, In: $5s^25p^1$, Sb: $5s^25p^3$, and Ni: $3d^94s^1$. To gain a better understanding on the structural stability from the chemical bonding perspective, the projected crystal orbital Hamilton populations (pCOHP) analysis was employed using the local orbital basis suite towards electronic-structure reconstruction (LOBSTER) code [34–37]. This method allows the extraction of chemical bonding information from prior DFT-based plane-wave electronic structure calculations. The analysis of atomic charge was performed via the Bader approach using VASP results [38].

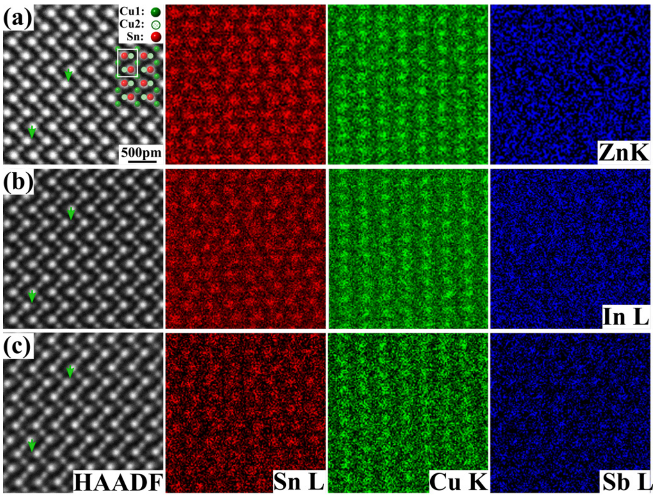

FIG. 2. HAADF images and corresponding original atomic-resolution elemental maps of (a) $Cu_6(Sn, Zn)_5$, (b) $Cu_6(Sn, In)_5$, (c) $Cu_6(Sn, Sb)_5$. The green arrows indicate the *Cu*2 sites at the peak shoulders of *Sn* sites in the HAADF images.

III. RESULTS

A. Direct evidence of dopant preferable sites via atomic-resolution STEM-XEDS mapping and analysis

Figure 2 shows a series of atomic-resolution HAADF images and XEDS maps, consistently acquired along the $[2\bar{1}\bar{1}0]$ direction of the hexagonal η-Cu_6Sn_5 crystal structure at room temperature. This projection view can distinguish the three atomic Wyckoff sites, namely *Cu*1, *Cu*2, and *Sn* in η-Cu_6Sn_5 as illustrated in Fig. 1(b), thus allowing the unambiguous identification of dopant positions in subsequent analysis. In contrast, *Cu*2 sites overlap with *Sn* sites along $[01\bar{1}0]$ and [0001] projections, as confirmed with red open circles in Figs. 1(c) and 1(d). Atomic columns of *Cu*1 and *Sn* sites are clearly distinguishable with a much brighter contrast in the latter, on the basis of *Z* contrast in the HAADF images in Fig. 2, owing to the difference in atomic number as $Z_{Cu} = 29$ and $Z_{Sn} = 50$ of the main components. Note that only 20% occupancy of *Cu*2 sites on average results in a much lower HAADF intensity compared to those at the *Cu*1 sites with full occupancy (Fig. 2). The corresponding intensity line profiles extracted from the HAADF images in Fig. 2 are shown in Fig. S2 of Ref. [33] where *Cu*2 sites can be found as shoulders of the peaks of *Sn* sites. The atomic locations of Zn, In, and Sb dopants are not identified in the current HAADF images due to the low concentration of ~4.5 at. %. We further confirmed

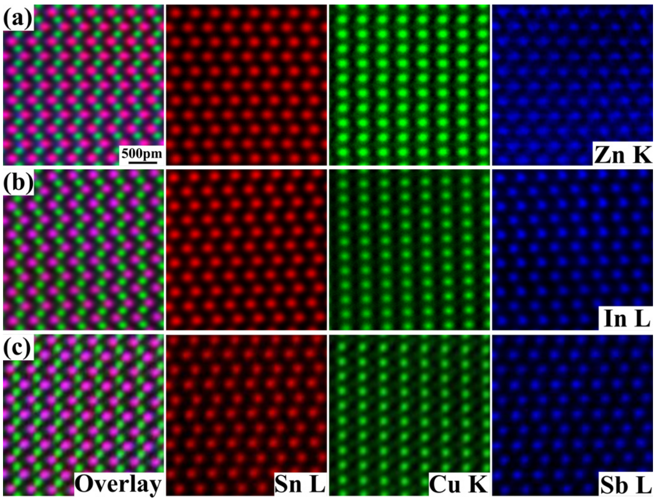

FIG. 3. Poisson NLCPA-processed atomic-resolution elemental maps of (a) $\mathrm{Cu_6(Sn,Zn)_5}$, (b) $\mathrm{Cu_6(Sn,In)_5}$, (c) $\mathrm{Cu_6(Sn,Sb)_5}$

columns of *Cu*1 and *Sn* sites in the XEDS elemental mappings at the atomic scale corresponding to the HAADF images, i.e., *Sn* periodically repeats in a zigzag fashion while Cu shows a rectangular pattern. However, only slightly discernible traces of In and Sb dopants appear in the XEDS maps while almost no significant information from Zn can be registered from the noisy map background. It is also notable that heavier dopants such as In and Sb are more efficient at x-ray production compared to Zn, thus appearing only faintly on the corresponding XEDS maps

Using two independent noise reduction methods as described above, we successfully improved the signal-to-noise ratios (SNRs) of all trace elements in the original XEDS maps. Indeed, the NLPCA-processed maps (Fig. 3) can resolve all dopants' weak XEDS signals including Zn, In, and Sb at the *Sn* sites in η-$\mathrm{Cu_6Sn_5}$ with excellent clarity, corresponding to the zigzag pattern of *Sn* columns. In addition, the lattice-averaged maps obtained in Fig. 4 further confirm the preferable occupancy of Zn, In, and Sb at the *Sn* sites in η-$\mathrm{Cu_6Sn_5}$ and are in excellent agreement with those processed by Poisson NLPCA. Notably, one may recognize the trace of Cu element at the *Cu*2 sites, although minor but evident, adjacent to the much brighter *Cu*1 sites in the Cu-*K* maps given its relatively low occupancy of Cu (20%). For ease of visualization, the intensity of dopants has been renormalized in Figs. 3 and 4. In summary, these results collectively provide direct and conclusive evidence on the atomic locations of dopants in η-$\mathrm{Cu_6Sn_5}$ using cutting-edge microscopy and image-processing algorithms.

B. Effect of dopant atomic positions on the energetics of η-$\mathrm{Cu_6Sn_5}$

The above STEM-XEDS results allow us to unambiguously identify the substitution of Zn, In, and Sb for *Sn* in η-$\mathrm{Cu_6Sn_5}$. In comparison to our previous work [28], Ni dopants, however, prefer the *Cu*2 sites. Importantly, all dopants play a certain role in the stabilization of the hexagonal η-$\mathrm{Cu_6Sn_5}$ down to room temperature, which otherwise would favor the transformation into the monoclinic η'-$\mathrm{Cu_6Sn_5}$ structure. We postulate that the origin of such behavior is closely related to the preferable atomic locations of dopant atoms in the η-$\mathrm{Cu_6Sn_5}$ lattices. To this end, we performed DFT calculations to gain further insights into the effect of dopant positions on the energetics of η-$\mathrm{Cu_6Sn_5}$. Particularly, the formation enthalpy (ΔH) is used to evaluate the stability of each structural model as follows:

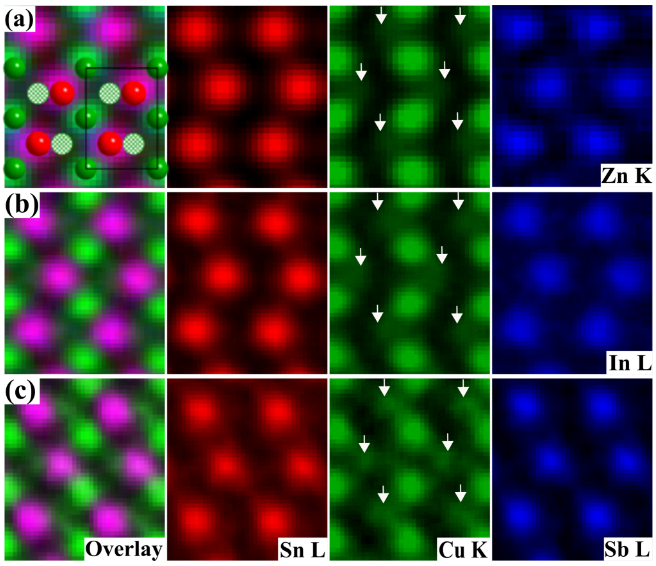

FIG. 4. Lattice-averaged maps of (a) $\mathrm{Cu_6(Sn,Zn)_5}$, (b) $\mathrm{Cu_6(Sn,In)_5}$, (c) $\mathrm{Cu_6(Sn,Sb)_5}$. The *Cu*2 sites are indicated by the white arrows in the Cu-*K* maps.

$$\Delta H = \frac{1}{88}\{E_{\mathrm{Cu}(48-x)\mathrm{Sn}(40-y)M(x+y)} + xE_{\mathrm{Cu}} + yE_{\mathrm{Sn}} - [E_{\mathrm{Cu48Sn40}} + (x+y)E_M\,]\}. \tag{1}$$

Here $E_{\mathrm{Cu}(48-x)\mathrm{Sn}(40-y)M(x+y)}$ and E_{Cu48Sn40} are the total energies of 2×2×5 supercells corresponding to η-$\mathrm{Cu_6Sn_5}$ with and without dopants, respectively. E_{Cu}, E_{Sn}, and E_M (M = Zn, Sb, In, Ni) are the total energy per atom of each constituent element in its pure crystalline form, *i.e.*, face-centered-cubic (fcc) Cu, tetragonal β-Sn, hcp Zn, tetragonal In, rhombohedral Sb, and fcc Ni. Note that by this definition, the ΔH value is zero for pure η-$\mathrm{Cu_6Sn_5}$.

Figure 5 summarizes the calculated enthalpies of formation for various hypothetical models $\mathrm{(Cu,}X\mathrm{)_6Sn_5}$ and $\mathrm{Cu_6(Sn,}X\mathrm{)_5}$ (X = Zn, In, Sb, Ni) corresponding to different dopant sites *Cu*1, *Cu*2, and *Sn*. We find that Zn and In appear the most energetically favorable at the *Sn*1 sites close to the *Cu*2 sites ($\Delta H = -21.1$ and -6.6 meV/atom for Zn and In, respectively) while Sb prefers the *Sn*3 sites away from the *Cu*2 sites ($\Delta H = 4.1$ meV/atom). Theoretically, the three *Sn* sites are crystallographically equivalent Wyckoff sites, corresponding to the minor energy differences as seen when In or Sb is located at either *Sn*1, *Sn*2, or *Sn*3 sites (Fig. 5). However, this energy variation is significant for the case of Zn and its occupancy at the *Sn*2 or *Sn*3 sites may result in an energetically unstable configuration. Such feature of Zn occupancy was consistently observed for three different random arrangements of *Cu*2 sites in η-$\mathrm{Cu_6Sn_5}$ as shown in Fig. S3 of Ref. [33]. In contrast to these three dopants, Ni at the *Cu*2 sites entails the lowest energy configurations ($\Delta H = -38.7$ meV/atom).

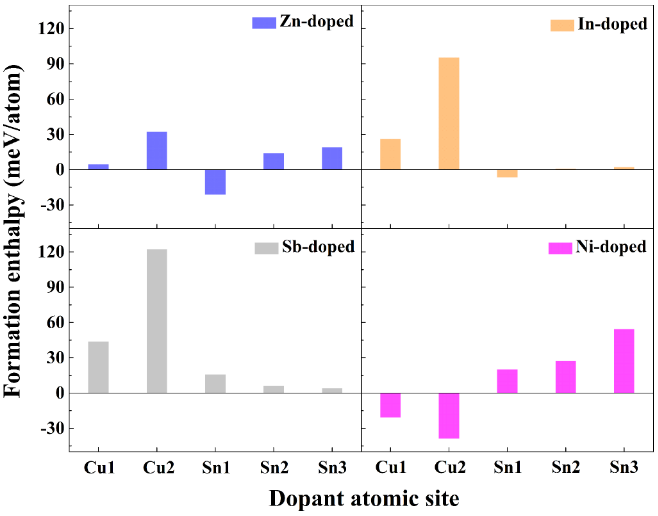

FIG. 5. The formation enthalpy of η-Cu$_6$Sn$_5$ with dopants at various Wyckoff sites.

It is also notable that *Cu*2 sites are amongst the least preferred locations for Zn, In, and Sb because of their relatively high energetics, in a corresponding manner of *Sn* sites to Ni dopant. Additional calculations have also been performed for a more dilute case using only one dopant atom in the same supercell models for excluding the effect of interaction between dopant atoms within the supercells. The results given in Fig. S4 of Ref. [33] show similar site preferences to those presented in Fig. 5. One can find additional discussion on the contribution of configurational entropy to the free energy in Ref. [33]. It is also worth noting that the configurational entropy at room temperature gives only very minor effects on the phase stability for all the dopant cases. In summary, the DFT results are consistent with our experimental XEDS finding although we did not observe the variation of Zn distribution among the *Sn* sites in Figs. 3 and 4, most likely due to the averaging effect of the random distribution of *Cu*2 sites in η-Cu$_6$Sn$_5$. Furthermore, the present results confirm the calculations of Schwingenschlögl *et al.* [26] and Chen *et al.* [39] for Ni preference at the *Cu*2 sites. In comparison, Zeng *et al.* [27] also hypothesized that Zn and In tend to occupy the *Sn* sites in η-Cu$_6$Sn$_5$ based on theoretical calculations. To our knowledge, no other reports on Sb dopants in η-Cu$_6$Sn$_5$ are currently available.

IV. DISCUSSION

Based on the initial screening of the most energetically stable η-Cu$_6$Sn$_5$ configurations for each dopant type, we further calculated the local density of states (LDOS) and projected crystal orbital Hamilton populations (pCOHP) associated with these configurations. Figure 6(a) illustrates the LDOS curves spanning an energy window of 16 eV enclosing the Fermi level. More details of the orbital projected density of states (PDOS) can be found in Fig. S5 of Ref. [33]. In the corresponding −pCOHP analysis [Fig. 6(b)], we considered the interatomic interactions between a dopant of interest with its nearest neighbors at the *Cu*1, *Cu*2, and *Sn* sites within a range between 1 and 4 Å. Note that bonding interactions correspond to −pCOHP > 0 while antibonding interactions occur for −pCOHP < 0. Likewise, zero values of −pCOHP denote nonbonding situations.

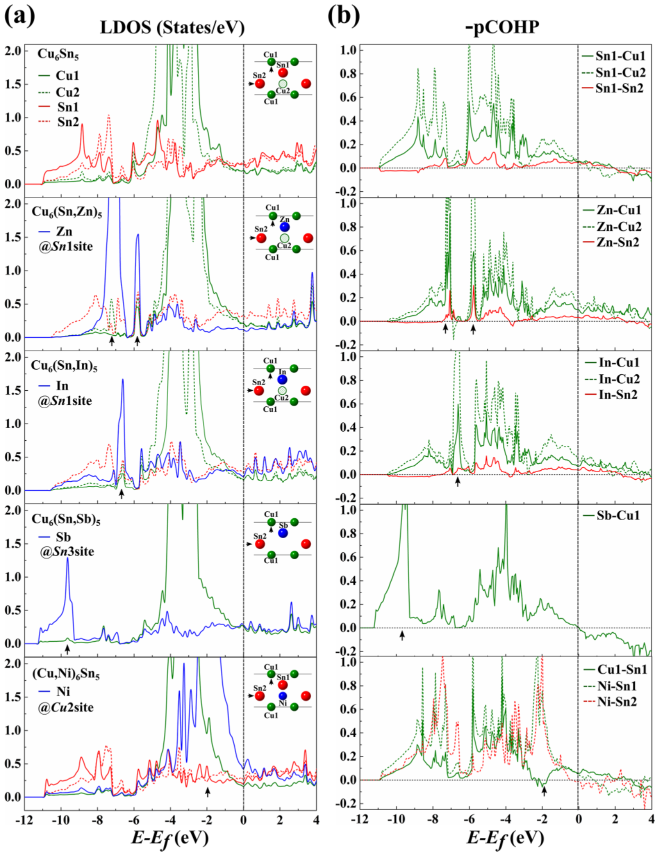

FIG. 6. (a) LDOS curves at the dopant sites and their nearest neighbors for η-Cu$_6$Sn$_5$ without/with dopants, (b) corresponding −pCOHP curves of selected pairwise interactions for η-Cu$_6$Sn$_5$ without/with dopants. Note that significant distinct interatomic interactions between Cu or *Sn* host atoms with the dopants are indicated by the arrows. The local atomic configurations around the dopant atoms are displayed along the $[2\bar{1}\bar{1}0]$ direction for clarity.

Generally, the finite local density of states (LDOS) values at the Fermi level characterize the metallic nature of the η-Cu$_6$Sn$_5$ intermetallic compounds. A prominent feature observed in all LDOS plots is the large contribution from Cu-3*d* states at both *Cu*1 and *Cu*2 sites in the valence-band region between −1 and −6 eV, suggesting its dominant influence on the overall interatomic interactions. Indeed, a major part of the overall bonding states can also be identified within this energy range in the corresponding −pCOHP curves [Fig. 6(b)]. While Sn-*s* exhibits a relatively smaller peak at about −7.5 eV below the Fermi level, other Cu-*s* and Sn-*p* orbitals form broad, free-electron-like energy bands. When comparing between the cases without and with dopants, we find additional distinct Cu and/or *Sn* LDOS peaks in the latter case, most probably due to orbital mixing between Cu and/or *Sn* with the dopant elements including Zn, In, and Sb [Fig. 6(a)]. These peaks agree well with those at the same energy level in the corresponding −pCOHP plots [Fig. 6(b)]. For instance, Zn-*d* and Zn-*s* develop hybridization with *Cu*2-*d* (i.e., Cu-*d* orbital on *Cu*2 site) and Sn2-*s*

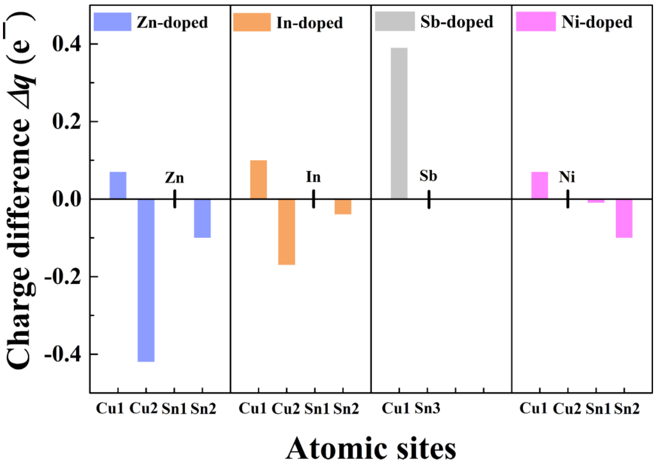

FIG. 7. Bader charge analysis for various atomic sites neighboring a dopant of interest with reference to the pure η-Cu_6Sn_5. Note that Sb is located at the *Sn*3 site surrounded by *Cu*1 atoms.

(i.e., Sn-*s* orbital on *Sn*2 site) at about −7.2 and −5.8 eV, respectively. On the other hand, *Cu*2-*d* overlaps with In-*s* at −6.7 eV giving rise to a strong hybridized orbital at this energy level. Finally, Sb-*s* states interact the most strongly with *Cu*1-*d* at −9.7 eV below the Fermi level. In contrast to other dopant cases, Ni at the *Cu*2 sites is associated with the strong hybridization between Ni-*d* and Sn1-*p* orbitals, appearing the most pronounced at −2 eV in both LDOS and −pCOHP curves. It is suggested that the development of distinct heteroatomic bonds between the dopants and host atoms is a favorable factor toward the stability of η-Cu_6Sn_5 at low temperatures.

To further evaluate the relative strength of different pairwise interactions, we examined the integrated −pCOHP (−IpCOHP), which is defined as an energy integral of the −pCOHP up to the Fermi level (E_F) [35] according to Eq. (2):

$$-\text{IpCOHP} = \int^{E_F} -\text{pCOHP}(E)\,dE. \tag{2}$$

It should also be noted that the −IpCOHP values between alloys with dissimilar compositions cannot be compared directly because the energy reference point based on the average electrostatic potential in each DFT-based calculation varies from one system to another [40]. Therefore, here we only compare the relative −IpCOHP values between different interactions within the same supercells, i.e., interactions involving a dopant and other equivalent interactions away from the dopant area. In addition, we analyzed the change in Bader atomic charge (Δq) for various atomic sites adjacent To the dopants of interest with reference to the pure η-Cu_6Sn_5 (Fig. 7). Note that a negative charge difference for an atomic site indicates a loss of valence electrons compared to an equivalent site in the pure η-Cu_6Sn_5, and vice versa.

For most of the selected pairwise interactions shown in Table II, an enhancement in bond strength is often regarded as enhanced by a bond-length reduction, occurring the most notably for Sb-Cu1, Ni-Sn1, and Ni-Sn2 pairs. Here Sb-Cu1 denotes the interaction between a Sb atom and a Cu atom at the *Cu*1 site, and so forth. However, for the case of Zn and In dopants, we observe a different bonding situation where direct bonds between Zn/In and Cu at the *Cu*2 sites are slightly destabilized along with the concurrent strengthening of the electronic bound states for *Cu*2-Sn neighbor pairs, possibly due to the effect of charge redistribution between Zn/In and Cu at the *Cu*2 sites. In fact, our Bader charge analysis indicates a local charge transfer of $\Delta q = 0.42$ and $0.17\,e^-$ from Cu at the *Cu*2 sites to its neighbors in the case of Zn and In dopant, respectively (Fig. 7). As a net effect, the overall bonding environments remain optimized, which yields an energy gain of the systems, corroborating with the lowest energy configurations for η-Cu_6Sn_5 with Zn/In at the *Sn*1 sites as previously discussed in Fig. 5. The same trend may be visualized more clearly in Fig. 8 in terms of the spatial distribution of charge density, corresponding to isosurface values up to $\Delta\rho_{\max} = 2.6\,e^-/\text{Å}^3$, when viewed along the $[2\bar{1}\bar{1}0]$ direction of the $1\times1\times5$ η-Cu_6Sn_5 supercells for all dopant cases (Fig. 8). Note that the high density of charge is generally indicative of a stronger chemical bond and significant bonding interactions are indicated by the arrows in Fig. 8.

Comparison of the energy difference (ΔE) between the η and η'-Cu_6Sn_5 with dopants located at the most favorable

TABLE II. Bond lengths and corresponding −IpCOHP values for selected pairwise interations in η-Cu_6Sn_5 without/with dopants after the structural optimization. Note that the values should be compared in a row-wise manner between equivalent interactions within the same atomic models.

Atomic model	Neighbors to dopants	Bond length (Å)	−IpCOHP (eV/bond)	Away from dopants	Bond length (Å)	−IpCOHP (eV/bond)
Dopant-free η-Cu_6Sn_5	NA	NA	NA	Cu2-Sn1	2.49	3.17
	NA	NA	NA	Cu2-Sn2	2.75	2.17
Zn-doped @ *Sn*1 site	Cu2-Zn	2.45	2.41	Cu2-Sn1	2.45	3.26
	Cu2-Sn2	2.63	2.60	Cu2-Sn2	2.78	2.03
In-doped @ *Sn*1 site	Cu2-In	2.49	2.79	Cu2-Sn1	2.49	3.18
	Cu2-Sn2	2.69	2.37	Cu2-Sn2	2.76	2.14
Sb-doped @ *Sn*3 site	Cu1-Sb	2.79	2.52	Cu1-Sn3	2.79	2.45
Ni-doped @ *Cu*2 site	Ni-Sn1	2.55	3.16	Cu2-Sn1	2.59	2.77
	Ni-Sn2	2.66	2.79	Cu2-Sn2	2.77	2.11

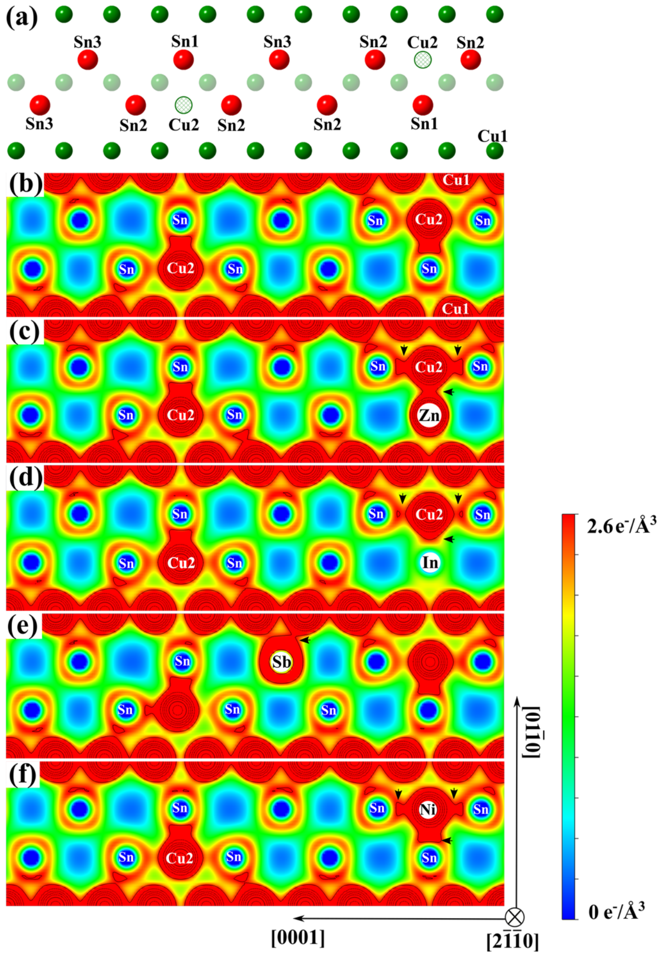

FIG. 8. (a) A 1×1×5 supercell model viewed along the [$2\bar{1}\bar{1}0$] direction for pure η-Cu_6Sn_5; corresponding charge density distribution profiles for (b) pure η-Cu_6Sn_5, (c) η-$Cu_6(Sn, Zn)_5$, (d) η-$Cu_6(Sn, In)_5$, (e) η-$Cu_6(Sn, Sb)_5$, and (f) η-$(Cu, Ni)_6Sn_5$.

atomic sites in each structural setting supports our arguments above (Table III). For the dopant-free Cu_6Sn_5, the η' phase is 0.78 eV lower in energy compared to the η analog at 0 K, consistent with the fact that the former is often found in real samples under ambient conditions. We note that our calculated value agrees well with another study [41] also employing VASP while those performed by Schwingenschlögl *et al.* [26] using the all-electron scheme, i.e., WIEN2K code, give a higher value of 1.21 eV for the same supercell settings. Although the absolute values may be the subject of debate due to the inherent accuracy of each computational code, a relative comparison is still deemed valid in the present case. Notably, we find that the energy gap (ΔE) between the η and η'-Cu_6Sn_5 is significantly reduced to 0.20, 0.54, 0.67, and 0.74 eV in the presence of Zn, Ni, In, and Sb dopants, respectively, without changing the original energy order. The energy gains in favor of the η-Cu_6Sn_5 are likely attributable to the hybridization effects induced by dopants as discussed above for the η-Cu_6Sn_5. Consequently, the driving force required for the transformation from the η to η'-Cu_6Sn_5 upon cooling is decreased, leading to the stabilization of the η-Cu_6Sn_5 at room temperature. Furthermore, on the basis of the energy difference (ΔE) and −IpCOHP bonding analysis, the effectiveness of each dopant for the stabilization of η-Cu_6Sn_5 is suggested in a descending order as follows: Zn > Ni > In > Sb.

V. CONCLUSION

In this paper, we have systematically investigated the atomic locations of various trace dopants in η-Cu_6Sn_5 using advanced microscopy coupled with sophisticated denoising algorithms and first-principles calculations. The main conclusions drawn from this study are as follows:

(1) Zn, In, and Sb dopant atoms are consistently identified at the Wyckoff *Sn* sites of η-Cu_6Sn_5 based on the results of atomic-resolution elemental STEM-XEDS and two independent noise reduction methods, namely Poisson NLPCA and symmetric lattice averaging. In comparison to our previous work, Ni is found at the *Cu*2 sites in η-Cu_6Sn_5.

(2) Using first-principles calculations and hypothetical structural models for η-Cu_6Sn_5, we find Zn or In substitution for *Sn* at the *Sn*1 sites, close to the *Cu*2 sites, lead to the lowest enthalpies of formation while Sb energetically prefers the *Sn*3 sites away from the *Cu*2 sites. The same argument is also applicable for Ni at the *Cu*2 sites.

(3) From the chemical bonding perspective, our LDOS and pCOHP analysis further reveals that Zn, In, and Sb develop noticeable orbital mixing with the 3*d* valence states of Cu host atoms while Ni interacts the most strongly with Sn-*p* states in η-Cu_6Sn_5, while most of these direct interactions lead to an enhancement in bonding strength, most notably for Sb-Cu1, Ni-Sn1, and Ni-Sn2 heteroatomic pairs. For the case of Zn and In, the situation differs by which the direct

TABLE III. Comparison of the energy difference (ΔE) between the η and η'-Cu_6Sn_5 with/without dopants.

	Total energy E (eV/ two formula units) (this work)		Energy difference $\Delta E = E_\eta - E_{\eta'}$ (eV)	
Atomic model	η-Cu_6Sn_5	η'-Cu_6Sn_5	This work	Others
Dopant free	−82.78	−83.56	0.78	0.80 [41], 1.21 [26]
Zn doped	−80.55 (Zn @ *Sn*1)	−80.75 (Zn @ *Sn*3′)	0.20	0.20 [41]
In doped	−81.69 (In @ *Sn*1)	−82.36 (In @ *Sn*3′)	0.67	NA
Sb doped	−83.03 (Sb @ *Sn*3)	−83.77 (Sb @ *Sn*2′)	0.74	NA
Ni doped	−85.37 (Ni @ *Cu*2)	−85.91 (Ni @ *Cu*4′)	0.54	0.90 [26]

Notes: While the *Cu*2 sites in η-Cu_6Sn_5 are crystallographically equivalent to the *Cu*4′ sites in η'-Cu_6Sn_5, there are no direct correlations between each of the *Sn* sites in η and those in η'. Hence, only the most energetically favorable sites for each dopant case are summarized here. Full calculations for all atomic sites in each structural setting can be found in Table S3 of Ref. [33].

bonds between the dopants with the Cu host atoms at the *Cu*2 sites are slightly destabilized while the electronic bound states for Cu2-Sn2 pairs neighboring to the dopants are significantly enhanced. This may be attributed to the complex Bader charge transfer from Cu at the *Cu*2 sites to their neighbors, and as a net effect, the overall bonding environments within the η-Cu_6Sn_5 supercells remain optimized. It is believed the formation of various heteroatomic interactions due to charge redistribution in the presence of dopants at certain atomic sites is an important factor governing the phase stability of η-Cu_6Sn_5.

(4) We also find the narrowing of the energy gaps (ΔE) between the η and η'-Cu_6Sn_5 with dopants located at the most favorable atomic sites in each structural setting. The driving force required for the transformation from the η to η'-Cu_6Sn_5 upon cooling is thus reduced, leading to the stabilization of η-Cu_6Sn_5 at room temperature.

ACKNOWLEDGMENTS

This work was supported by the Progress 100 program at Kyushu University (KU) and a "UQ-KU project" at the University of Queensland (UQ), which assists research collaborations between UQ and KU. The authors thank X. Tan and S. Liu at The University of Queensland (UQ) for sample preparation. W.Y. was financially supported by a China Scholarship Council (CSC) Scholarship.

[1] T. Laurila, V. Vuorinen, and M. Paulasto-Kröckel, Impurity and alloying effects on interfacial reaction layers in pb-free soldering, Mater. Sci. Eng. R Rep. **68**, 1 (2010).

[2] D. K. Mu, S. D. McDonald, J. Read, H. Huang, and K. Nogita, Critical properties of Cu_6Sn_5 in electronic devices: Recent progress and a review, Curr. Opin. Solid State Mater. Sci. **20**, 55 (2016).

[3] T. Y. Lee, W. J. Choi, K. N. Tu, J. W. Jang, S. M. Kuo, J. K. Lin, D. R. Frear, K. Zeng, and J. K. Kivilahti, Morphology, kinetics, and thermodynamics of solid-state aging of eutectic SnPb and Pb-free solders (Sn–3.5 Ag, Sn–3.8 Ag–0.7 Cu and Sn–0.7 Cu) on Cu, J. Mater. Res. **17**, 291 (2002).

[4] A.-K. Larsson, L. Stenberg, and S. Lidin, The superstructure of domain-twinned η';-Cu_6Sn_5, Acta Cryst. B **50**, 636 (1994).

[5] A. K. Larsson, L. Stenberg, and S. Lidin, Crystal structure modulations in η; -Cu_5Sn_4, Z. Kristallogr. **210**, 832 (1995).

[6] Y. Q. Wu, J. C. Barry, T. Yamamoto, Q. F. Gu, S. D. McDonald, S. Matsumura, H. Huang, and K. Nogita, A new phase in stoichiometric Cu_6Sn_5, Acta Mater. **60**, 6581 (2012).

[7] K. Nogita, C. M. Gourlay, S. D. McDonald, Y. Q. Wu, J. Read, and Q. F. Gu, Kinetics of the η; $-\eta'$; transformation in Cu_6Sn_5, Scr. Mater. **65**, 922 (2011).

[8] K. Nogita, S. D. McDonald, H. Tsukamoto, J. Read, S. Suenaga, and T. Nishimura, Inhibiting cracking of interfacial Cu_6Sn_5 by Ni additions to Sn-based lead-free solders, Trans. Jpn. Inst. Electron. Packag. **2**, 46 (2009).

[9] T. Ventura, S. Terzi, M. Rappaz, and A. K. Dahle, Effects of solidification kinetics on microstructure formation in binary Sn–Cu solder alloys, Acta Mater. **59**, 1651 (2011).

[10] K. Nogita, D. Mu, S. D. McDonald, J. Read, and Y. Q. Wu, Effect of Ni on phase stability and thermal expansion of $Cu_{6-x}Ni_xSn_5$ ($X = 0$, 0.5, 1, 1.5 and 2), Intermetallics **26**, 78 (2012).

[11] N. Zhao, H. Ma, and L. Wang, Interfacial reactions between Sn-Cu based multicomponent solders and Ni substrates during soldering and aging, Solder. Surf. Mt. Technol. **21**, 19 (2009).

[12] C. M. Gourlay, J. Read, K. Nogita, and A. K. Dahle, The maximum fluidity length of solidifying Sn-Cu-Ag-Ni solder alloys, J. Electron. Mater. **37**, 51 (2008).

[13] C. M. Gourlay, K. Nogita, J. Read, and A. K. Dahle, Intermetallic formation and fluidity in Sn-rich Sn-Cu-Ni alloys, J. Electron. Mater. **39**, 56 (2010).

[14] S. H. Wu, Y. J. Hu, C. T. Lu, T. S. Huang, Y. H. Chang, and C. Y. Liu, Electromigration study on Sn (Cu) solder/Ni (P) joint interfaces, J. Electron. Mater. **41**, 3342 (2012).

[15] H. Tsukamoto, Z. Dong, H. Huang, T. Nishimura, and K. Nogita, Nanoindentation characterization of intermetallic compounds formed between Sn–Cu (–Ni) ball grid arrays and Cu substrates, Mater. Sci. Eng. B **164**, 44 (2009).

[16] D. Mu, H. Huang, S. D. McDonald, J. Read, and K. Nogita, Investigating the mechanical properties, creep and crack pattern of Cu_6Sn_5 and $(Cu, Ni)_6Sn_5$ on diverse crystal planes, Mater. Sci. Eng. A **566**, 126 (2013).

[17] C. Y. Yu and J. G. Duh, Stabilization of hexagonal $Cu_6(Sn, Zn)_5$ by minor Zn doping of Sn-based solder joints, Scr. Mater. **65**, 783 (2011).

[18] G. Zeng, S. D. McDonald, Q. Gu, Y. Terada, K. Uesugi, H. Yasuda, and K. Nogita, The influence of Ni and Zn additions on microstructure and phase transformations in Sn–0.7 Cu/Cu solder joints, Acta Mater. **83**, 357 (2015).

[19] K. D. Kepler, J. T. Vaughey, and M. Thackeray, $Li_xCu_6Sn_5$ ($0 < x < 13$): An intermetallic insertion electrode for rechargeable lithium batteries, Electrochem. Solid State Lett. **2**(7), 307 (1999).

[20] Y. Xing, S. Wang, B. Fang, Y. Feng, and S. Zhang, Three-dimensional nanoporous Cu_6Sn_5/Cu composite from dealloying as anode for lithium ion batteries, Micropor. Mesopor. Mater. **261**, 237 (2018).

[21] S. Naille, R. Dedryvere, H. Martinez, S. Leroy, P.-E. Lippens, J.-C. Jumas, and D. Gonbeau, XPS study of electrode/electrolyte interfaces of η;-Cu_6Sn_5 electrodes in Li-ion batteries, J. Power Sources **174**, 1086 (2007).

[22] X. F. Tan, S. D. McDonald, Q. Gu, Y. Hu, L. Wang, S. Matsumura, T. Nishimura, and K. Nogita, Characterisation of lithium-ion battery anodes fabricated via in-situ Cu_6Sn_5 growth on a copper current collector, J. Power Sources **415**, 50 (2019).

[23] J. Zhang, Y. Zhang, X. Zhang, and Y. Xia, $Ni_xCu_{6-x}Sn_5$ alloys as negative electrode materials for rechargeable lithium batteries, J. Power Sources **167**, 171 (2007).

[24] J. Zhang, X. Zhang, and Y. Xia, Co-Doped $Co_xCu_{6-x}Sn_5$ alloys as negative electrode materials for rechargeable lithium batteries, J. Electrochem. Soc. **154**, A7 (2007).

[25] X.-Y. Fan, F.-S. Ke, G.-Z. Wei, L. Huang, and S.-G. Sun, Microspherical Cu_6Sn_5 alloy anode for lithium-ion battery, Electrochem. Solid-State Lett. **11**(11), A195 (2008).

[26] U. Schwingenschlögl, C. Di Paola, K. Nogita, and C. M. Gourlay, The influence of Ni additions on the relative stability of η; and η';-Cu_6Sn_5, Appl. Phys. Lett. **96**, 61908 (2010).

[27] G. Zeng, S. D. McDonald, Q. Gu, S. Suenaga, Y. Zhang, J. Chen, and K. Nogita, Phase stability and thermal expansion behavior of Cu_6Sn_5 intermetallics doped with Zn, Au and In, Intermetallics **43**, 85 (2013).

[28] W. Yang, T. Yamamoto, K. Aso, F. Somidin, K. Nogita, and S. Matsumura, Atom locations in a Ni doped η;-$(Cu, Ni)_6Sn_5$ intermetallic compound, Scr. Mater. **158**, 1 (2019).

[29] J. Salmon, Z. Harmany, C.-A. Deledalle, and R. Willett, Poisson noise reduction with non-local PCA, J. Math. Imaging Vis. **48**, 279 (2014).

[30] A. B. Yankovich, C. Zhang, A. Oh, T. J. A. Slater, F. Azough, R. Freer, S. J. Haigh, R. Willett, and P. M. Voyles, Non-rigid registration and non-local principle component analysis to improve electron microscopy spectrum images, Nanotechnology **27**, 364001 (2016).

[31] P. Lu, L. Zhou, M. J. Kramer, and D. J. Smith, Atomic-scale chemical imaging and quantification of metallic alloy structures by energy-dispersive X-ray spectroscopy, Sci. Rep. **4**, 3945 (2014).

[32] A. Westgren and G. Phragmen, X-ray analysis of copper-tin alloys, Z. Anorg. Allg. Chem. **175**, 80 (1928).

[33] See Supplemental Material at http://link.aps.org/supplemental/10.1103/PhysRevMaterials.4.065002 for the calculation of Cu_6Sn_5.

[34] R. Dronskowski and P. E. Blöchl, Crystal orbital Hamilton populations (COHP): Energy-resolved visualization of chemical bonding in solids based on density-functional calculations, J. Phys. Chem. **97**, 8617 (1993).

[35] V. L. Deringer, A. L. Tchougréeff, and R. Dronskowski, Crystal orbital Hamilton population (COHP) analysis as projected from plane-wave basis sets, J. Phys. Chem. A **115**, 5461 (2011).

[36] S. Maintz, V. L. Deringer, A. L. Tchougréeff, and R. Dronskowski, Analytic projection from plane-wave and PAW wavefunctions and application to chemical-bonding analysis in solids, J. Comput. Chem. **34**, 2557 (2013).

[37] S. Maintz, V. L. Deringer, A. L. Tchougréeff, and R. Dronskowski, LOBSTER: A tool to extract chemical bonding from plane-wave based DFT, J. Comput. Chem. **37**, 1030 (2016).

[38] W. Tang, E. Sanville, and G. Henkelman, A grid-based Bader analysis algorithm without lattice bias, J. Phys.: Condens. Matter **21**, 84204 (2009).

[39] S. Chen, W. Zhou, and P. Wu, The structural, elastic, electronic and thermodynamic properties of hexagonal $\eta; -Cu_{6-x}Ni_xSn_5$ ($x = 0$, 0.5, 1, 1.5 and 2) intermetallic compounds, Intermetallics **54**, 187 (2014).

[40] S. Steinberg and R. Dronskowski, The crystal orbital Hamilton population (COHP) method as a tool to visualize and analyze chemical bonding in intermetallic compounds, Crystals **8**, 225 (2018).

[41] Z. Wei and L. Yan-Yu, Stabilization of $\eta; -Cu_6Sn_5$ intermetallic compound by zn addition: first-principles investigation, Chin. Phys. Lett. **31**, 57101 (2014).